

**Magnetic interaction of Janus magnetic particles suspended in a viscous fluid**

Yujin Seong and Tae Gon Kang\*

*School of Aerospace and Mechanical Engineering, Korea Aerospace University, Goyang-si, Gyeonggi-do 412-792, Republic of Korea*

Martien A. Hulsen, Jaap M. J. den Toonder, and Patrick D. Anderson

*Department of Mechanical Engineering, Eindhoven University of Technology, P. O. Box 513, 5600 MB Eindhoven, The Netherlands*

(Received 9 December 2015; published 22 February 2016)

We studied the magnetic interaction between circular Janus magnetic particles suspended in a Newtonian fluid under the influence of an externally applied uniform magnetic field. The particles are equally compartmentalized into paramagnetic and nonmagnetic sides. A direct numerical scheme is employed to solve the magnetic particulate flow in the Stokes flow regime. Upon applying the magnetic field, contrary to isotropic paramagnetic particles, a single Janus particle can rotate due to the magnetic torque created by the magnetic anisotropy of the particle. In a two-particle problem, the orientation of each particle is found to be an additional factor that affects the critical angle separating the nature of magnetic interaction. Using multiparticle problems, we show that the orientation of the particles has a significant influence on the dynamics of the particles, the fluid flow induced by the actuated particles, and the final conformation of the particles. Straight and staggered chain structures observed experimentally can be reproduced numerically in a multiple particle problem.

DOI: [10.1103/PhysRevE.93.022607](https://doi.org/10.1103/PhysRevE.93.022607)**I. INTRODUCTION**

Integrated microfluidic systems utilizing magnetic particles have drawn attention because of their potential chemical and biomedical applications [1–4]. In these systems, functionalized magnetic particles have been adopted for use as actuators, stirrers to enhance mixing, capturers and carriers of target analytes, and biosensors for diagnostic applications. Unlike electric forces, the magnetic forces acting on the magnetic particles are insensitive to the electrochemical conditions of a surrounding fluid. Thus, the magnetic particles can be manipulated in a more predictable manner. Spherical particles with uniform magnetic properties (without magnetic anisotropy) are typically used for magnetic particle-based microfluidic systems.

For more advanced tasks such as the creation of building blocks for photonic crystals, tissue engineering, and microelectronic architecture, targeted assembly structures for specific applications become important [5,6]. Anisotropic particles, categorized by shape-anisotropic particles, chemically patterned particles, and internally structured particles, are fabricated to meet such needs. These particles exhibit more complex interparticle interactions and self-assembly structures than those observed in isotropic particles, enabling them to overcome limits that constrain the use of isotropic particles. Among anisotropic particles, Janus particles, named after the Roman god Janus, are unique because they provide asymmetry and directionality in a single particle [7].

A Janus (anisotropic) magnetic particle is composed of two different magnetic materials, e.g., a magnetic particle with a nonmagnetic cap, a nonmagnetic particle with a magnetic cap, and a particle with a magnetic hemisphere [8–10]. By coating one hemisphere of a particle with a thin layer of metal and the other hemisphere with a fluorescent material, the particle

rotates in response to a rotating external field. Such a particle can be utilized as a rheological probe [8]. Janus particles with a magnetic hemisphere are able to load chemical or biological payloads such as dyes, fluorophores, proteins, or cells. This facilitates applications such as detection in magnetic resonance imaging, separation, and drug delivery in the biomedical field. Nonspherical Janus particles such as Janus ellipsoids, Janus dumbbells, and Janus cylinders can also be fabricated to meet specific needs [11–13]. For more details on the synthesis, self-assembly, properties, and applications of Janus particles, we refer to two review articles [14,15].

Upon applying a uniform field, isotropic magnetic particles form linear chain structures due to magnetic interactions among the particles [16,17]. Janus magnetic particles, meanwhile, form chiral chains, staggered chains, or doubled chain-like structures as well as linear chain structures, depending on their internal structure [9,18–23]. In the presence of a rotating magnetic field, magnetic Janus colloids are found to form unusual crystal structures [24]. The type of magnetic material (paramagnetic or ferromagnetic), the type of externally applied field (static or dynamic), the magnetic susceptibility, the shape of particles, and the confinement of magnetic material within a particle can influence field-induced structure formation.

From a fundamental point of view, magnetic interaction among anisotropic particles is an important subject in the area utilizing Janus magnetic particles. In addition, the inclusion of hydrodynamic interaction is crucial to accurately predict the particle dynamics, even in simple two-particle magnetic interactions [25]. Most research on the magnetic interaction and self-assembly of Janus particles relies on experimentation. Even though modeling and simulation are employed to investigate the self-assembly and the dynamics of Janus particles [26–31], further studies are still required to understand the magnetic interaction lying behind the formation of various self-assembly structures and the fluid flow induced by the actuated particles. Direct numerical simulation schemes

\*Corresponding author: [tgkang@kau.ac.kr](mailto:tgkang@kau.ac.kr)

[32–37], which have been developed to solve particulate flows with isotropic magnetic particles, are promising options in tackling particulate flows with Janus magnetic particles if they are enhanced to take into account the magnetic anisotropy of the particles.

In this study, a previously developed two-dimensional numerical scheme [36] is enhanced to treat the magnetic anisotropy of the particles. To the best of our knowledge, this is the first attempt to apply the direct simulation scheme to solve particulate flows with suspended Janus magnetic particles. First, the developed numerical scheme is validated using a single-particle problem. Then we investigate the magnetic interaction between two circular Janus particles under the influence of an externally applied magnetic field. In three-particle interaction, the main focus will be on the effect of the orientation and the spatial configuration of the particles on particle dynamics, chain structures formed by the particles, and the flow induced by the actuated particles. Finally, we introduce the self-assembly in a multiparticle problem and compare numerical results with those reported in a previous experimental study.

## II. MODELING

### A. Problem definition

The problem we wish to solve is a two-dimensional particulate flow with monodisperse circular Janus magnetic particles suspended in a viscous fluid under the influence of an externally applied uniform magnetic field  $\vec{H}$ . The Janus particles used in simulations are equally compartmentalized into paramagnetic and nonmagnetic sides, which correspond to two-dimensional counterparts of spherical Janus particles presented in Ref. [9]. Half of a particle is made of a paramagnetic material with a constant magnetic permeability and the other half is made of a nonmagnetic material, leading to magnetic anisotropy and, consequently, unique behavior in an externally applied magnetic field. Our problem is associated with a real system where both the applied field and the normal directions to the internal interfaces of the particles are parallel to the plane on which the particles move.

Since we are concerned with Janus particles that are a few microns in size, the particles are assumed to be non-Brownian and inertialess. The magnetic permeability of the magnetic area is  $\mu_p$ , and that of the nonmagnetic area is  $\mu_0$ , where  $\mu_0$  is the permeability in vacuum and  $\mu_p > \mu_0$ . In addition, we assume a linear relation between the magnetic field and the induced magnetic moment, neglecting magnetic saturation, and solve magnetostatics [38]. The fluid is assumed to be nonmagnetic with the permeability  $\mu_0$  and Newtonian with a constant viscosity  $\eta$ . Since typical flows in microfluidic devices belong to the Stokes flow regime, the fluid flow is governed only by viscous forces and magnetic forces.

Figure 1 depicts a representative problem to be solved. The computational domain is a rectangular chamber filled with a fluid and Janus particles all with the same radius  $a$  suspended in the fluid. The chamber is  $2w$  wide and  $2h$  high. The four boundaries of the chamber are represented by  $\Gamma_1$ ,  $\Gamma_2$ ,  $\Gamma_3$ , and  $\Gamma_4$ . The origin of the coordinate system  $(x, y)$  is located at the center of the chamber that is periodic in the horizontal direction. The two boundaries,  $\Gamma_1$  and  $\Gamma_3$ , are stationary walls.

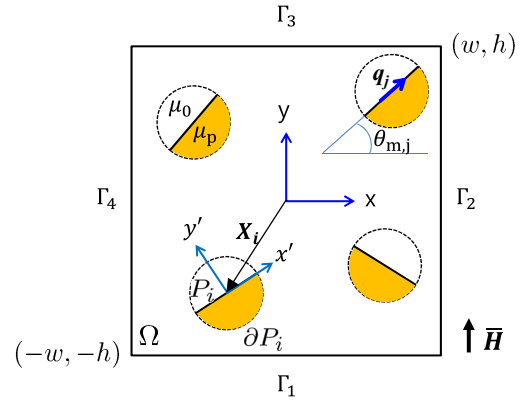


FIG. 1. Schematic representation of the problem with Janus magnetic particles suspended in a liquid under the influence of an externally applied magnetic field,  $\vec{H} = H_0 \mathbf{j}$ , where  $H_0$  is the magnitude of the field and  $\mathbf{j}$  is the unit vector along the  $y$  direction. In each particle, the area shaded in orange is the magnetic domain of the particle.

$P_i(t)$  denotes the area occupied by a particle at time  $t$ . The internal boundary separating magnetic and nonmagnetic areas in the particle is denoted by  $\partial P_i'$  and the outer boundary of the particle by  $\partial P_i$ . The collective region occupied by all the particles is defined by  $P(t) = \bigcup_{i=1}^N P_i(t)$ , where  $N$  is the number of particles. The fluid domain is denoted by  $\Omega \setminus P(t)$  with  $\Omega$  being the entire domain.

A local coordinate system  $(x'_i, y'_i)$ , which moves with the rigid-body motion of a particle  $P_i$ , is defined to represent the orientation of the particle. The origin of the local coordinate system is located at the center of the particle. A unit vector  $\mathbf{q}_i$  in the direction of the  $x'_i$  axis is employed as the orientation vector for the particle, defined by  $\mathbf{q}_i = \cos(\theta_{m,i})\mathbf{i} + \sin(\theta_{m,i})\mathbf{j}$ , where  $\mathbf{i}$  and  $\mathbf{j}$  are unit vectors along the  $x$  axis and  $y$  axis, respectively, and  $\theta_{m,i}$  is the orientation angle of the particle.

### B. Governing equations

In this section, we address the governing equations and corresponding boundary conditions for two-dimensional magnetic and flow problems, focusing on the way to treat the magnetic anisotropy of the Janus particle in both problems. For other information on modeling magnetic particulate flows, we refer to our previous works [33,37].

First, a magnetic problem is solved to obtain the magnetic field in the entire domain  $\Omega$  including the particles and the fluid. In magnetostatics without free current, the governing equation for the magnetic problem is given by

$$\nabla \cdot (\mu \nabla \phi) = 0, \quad (1)$$

where  $\phi$  is the magnetic scalar potential and  $\mu$  the magnetic permeability that is related to the magnetic susceptibility  $\chi$  by  $\mu = \mu_0(1 + \chi)$ . The externally applied magnetic field  $\vec{H}$  is imposed using constraints given by

$$\phi(-w, y) = \phi(w, y) + \Delta \phi_x, \quad \text{on } \Gamma_2 \cup \Gamma_4, \quad (2)$$

$$\phi(x, -h) = \phi(x, h) + \Delta \phi_y, \quad \text{on } \Gamma_1 \cup \Gamma_3, \quad (3)$$

where  $\Delta\phi_x$  is the potential difference between  $\Gamma_2$  and  $\Gamma_4$  and  $\Delta\phi_y$  that between  $\Gamma_1$  and  $\Gamma_3$ . The two potential differences are related to the components of  $\bar{\mathbf{H}}$  by  $H_x = \Delta\phi_x/2w$  and  $H_y = \Delta\phi_y/2h$ . A reference potential ( $\phi = 0$ ) is specified at one point  $\Gamma_p$  in the domain. Once the magnetic potential is obtained, it can be used to calculate the magnetic field intensity  $\mathbf{H}$  and the magnetic flux density  $\mathbf{B}$ , defined by  $\mathbf{H} = -\nabla\phi$  and  $\mathbf{B} = \mu\mathbf{H}$ , respectively.

The magnetic permeability  $\mu$  is discontinuous across the interface between the fluid and the outer boundary of the magnetic domain in a particle. In addition, the magnetic

permeability is not uniform in a particle but discontinuous across the internal interface  $\partial P_i'$  between magnetic and nonmagnetic domains. The magnetic permeability is evaluated using the local coordinate system defined in each particle and the signed distance function  $\delta(\mathbf{x})$  at a spatial position  $\mathbf{x}$ . The distance function is defined by  $\delta(\mathbf{x}) = \min\{|\mathbf{x} - \mathbf{X}_i| - R_i\}$  ( $i = 1, \dots, N$ ), where  $\mathbf{X}_i$  is the position vector to the center of the  $i^{\text{th}}$  particle and  $R_i$  the radius of the particle. As depicted in Fig. 1, the magnetic and nonmagnetic areas of a Janus particle  $P_i$  are divided by the  $x_i'$  axis. Therefore, the magnetic permeability at a position  $\mathbf{x}$  can be evaluated by

$$\mu(\mathbf{x}) = \begin{cases} \mu_0 & \text{if } \delta(\mathbf{x}) > 0 \text{ (fluid domain),} \\ \mu_p & \text{else if } \delta(\mathbf{x}) \leq 0 \text{ and } y_i'(\mathbf{x}) \leq 0 \text{ (magnetic area in } P_i), \\ \mu_0 & \text{otherwise (non-magnetic area in a particle).} \end{cases} \quad (4)$$

As for the flow in the Stokes flow regime, the continuity and the momentum balance equations in the fluid domain  $\Omega \setminus P(t)$  are given by

$$\nabla \cdot \mathbf{u} = 0, \quad (5)$$

$$\nabla \cdot \boldsymbol{\sigma} + \nabla \cdot \mathbf{T}_m = \mathbf{0}, \quad (6)$$

where  $\mathbf{u}$  is the velocity,  $\boldsymbol{\sigma}$  the Cauchy stress tensor, and  $\mathbf{T}_m$  the Maxwell stress tensor. The two stress tensors are defined by  $\boldsymbol{\sigma} = -p\mathbf{I} + \eta(\nabla\mathbf{u} + (\nabla\mathbf{u})^T)$  and  $\mathbf{T}_m = \mu(\mathbf{H}\mathbf{H} - H^2\mathbf{I}/2)$ , where  $p$  is the pressure,  $\eta$  the viscosity,  $\mathbf{I}$  the identity tensor, and  $H^2 = \mathbf{H} \cdot \mathbf{H}$ . The magnetic force is represented by the divergence of the Maxwell stress tensor, added as an additional body force to the momentum balance equation. No-slip condition is imposed on the bottom ( $\Gamma_1$ ) and top ( $\Gamma_3$ ) boundaries. The constraints for the horizontal periodicity between the two boundaries ( $\Gamma_2$  and  $\Gamma_4$ ) are represented by

$$\mathbf{u}(-w, y) = \mathbf{u}(w, y), \quad (7)$$

$$\mathbf{t}(-w, y) = -\mathbf{t}(w, y), \quad (8)$$

where  $\mathbf{t}$  is the traction defined by  $\mathbf{t} = \boldsymbol{\sigma} \cdot \mathbf{n}$ , where  $\mathbf{n}$  is the outward unit normal vector at the boundaries.

To treat the rigid-body constraints for particles with nonuniform magnetic properties, a *modified rigid-ring description* is employed for the particle domain  $P(t)$ . In this model, the fluid also fills the particle domain, as used in the original rigid-ring description [39]. But the rigid-body constraints should be imposed on the internal boundary  $\partial P_i'$  as well as the particle boundary  $\partial P_i$ , given by

$$\mathbf{u} = \mathbf{U}_i + \boldsymbol{\omega}_i \times \mathbf{r}_i, \quad (9)$$

where  $\mathbf{U}_i$  is the translational velocity of the  $i^{\text{th}}$  particle,  $\boldsymbol{\omega}_i$  the angular velocity of the particle, and  $\mathbf{r}_i = \mathbf{x} - \mathbf{X}_i$ . In the two-dimensional case,  $\boldsymbol{\omega}_i = \omega_i \mathbf{k}$ , where  $\mathbf{k}$  is the unit vector perpendicular to the  $xy$  plane and  $\omega_i$  the magnitude of the angular velocity. In this manner, we are able to solve the same governing equations for the whole domain  $\Omega$ .

After solving the set of governing equations for the flow problem, one can determine the unknown rigid-body motions

( $\mathbf{U}_i, \omega_i$ ) of the particles as well as the velocity  $\mathbf{u}$  and pressure  $p$ . Using the rigid-body motions at time  $t$ , the position  $\mathbf{X}_i$  and the angle  $\theta_{m,i}$  of the particles are updated by solving the evolution equations, represented by

$$\frac{d\mathbf{X}_i}{dt} = \mathbf{U}_i, \quad \mathbf{X}_i(0) = \mathbf{X}_i^0, \quad (10)$$

$$\frac{d\theta_{m,i}}{dt} = \omega_i, \quad \theta_{m,i}(0) = \theta_{m,i}^0, \quad (11)$$

where  $\mathbf{X}_i^0$  and  $\theta_{m,i}^0$  are the initial position vector and the initial orientation angle of the  $i^{\text{th}}$  particle, respectively. Then, for a new particle configuration, the solution procedure of solving the two problems is repeated to the time one want to analyze.

### III. NUMERICAL METHODS

To solve the particulate flow with Janus magnetic particles, in this study, we enhanced our previous method to be able to account for the magnetic anisotropy of the Janus particles. Compared with the method introduced in the previous studies [32,36,37], the major differences are in the treatment of the magnetic anisotropy of the particles dependent on their orientations and the use of the modified rigid-ring description implemented by means of Lagrange multipliers. Introduced below are the weak forms to solve the two-dimensional magnetic particulate flow with circular Janus magnetic particles.

The weak form for the magnetic problem, governed by the set of equations [Eqs. (1)–(3)] for the magnetic potential  $\phi$ , is given as:

$$\int_{\Omega} \mu \nabla \phi \cdot \nabla \psi dA + \langle \lambda^{m,h}, \psi(-w, y) - \psi(w, y) \rangle_{\Gamma_4} + \langle \lambda^{m,v}, \psi(x, -h) - \psi(x, h) \rangle_{\Gamma_1} = 0, \quad (12)$$

$$\langle \mu^{m,h}, \phi(-w, y) - \phi(w, y) \rangle_{\Gamma_4} = \langle \mu^{m,h}, \Delta\phi_x \rangle_{\Gamma_4}, \quad (13)$$

$$\langle \mu^{m,v}, \phi(x, -h) - \phi(x, h) \rangle_{\Gamma_1} = \langle \mu^{m,v}, \Delta\phi_y \rangle_{\Gamma_1}, \quad (14)$$

where  $\psi$  is the weighting function for the potential,  $\lambda^{m,h}$  and  $\lambda^{m,v}$  are the Lagrange multipliers for the two constraints

[Eqs. (2) and (3)], respectively, and  $\mu^{m,h}$  and  $\mu^{m,v}$  the weighting functions for the two Lagrange multipliers,  $\lambda^{m,h}$  and  $\lambda^{m,v}$ , respectively. We use biquadratic interpolation for the potential and linear interpolations for the Lagrange multipliers. When integrating the first term in Eq. (12), the magnetic permeability  $\mu$  at a quadrature point  $\mathbf{x}_q$  is evaluated by Eq. (4) using the distance function  $\delta(\mathbf{x}_q)$  and the local coordinate  $y'_i(\mathbf{x}_q)$  (if the quadrature point  $\mathbf{x}_q$  is inside a particle  $P_i$ ). Using a sparse Gauss elimination method, HSL/MA57 [40], the resulting matrix equation is solved to find the potential in the entire domain.

The flow problem is solved by using a finite-element-based fictitious domain method [37]. Fluid-particle and particle-particle hydrodynamic interactions are treated implicitly through a combined weak form for the flow problem, given by

$$\begin{aligned} & \int_{\Omega} 2\eta \mathbf{D}(\mathbf{v}) : \mathbf{D}(\mathbf{u}) dA - \int_{\Omega} (\nabla \cdot \mathbf{v}) p dA \\ & + \sum_{i=1}^N \langle \mathbf{v} - (\mathbf{V}_i + \boldsymbol{\chi}_i \times \mathbf{r}_i), \boldsymbol{\lambda}^{p,i} \rangle_{\partial P_i \cup \partial P'_i} \\ & + \langle \boldsymbol{\lambda}^h, \mathbf{v}(-w, y) - \mathbf{v}(w, y) \rangle_{\Gamma_4} = - \int_{\Omega} \mathbf{D}(\mathbf{v}) : \mathbf{T}_m dA, \end{aligned} \quad (15)$$

$$- \int_{\Omega} q (\nabla \cdot \mathbf{u}) dA = 0, \quad (16)$$

$$\langle \boldsymbol{\mu}^{p,i}(\mathbf{x}), \mathbf{u}(\mathbf{x}) - (\mathbf{U}_i + \boldsymbol{\omega}_i \times \mathbf{r}_i) \rangle_{\partial P_i \cup \partial P'_i} = 0, \quad (17)$$

$$\langle \boldsymbol{\mu}^h, \mathbf{u}(-w, y) - \mathbf{u}(w, y) \rangle_{\Gamma_4} = 0, \quad (18)$$

where  $\mathbf{v}$ ,  $q$ ,  $\mathbf{V}_i$ ,  $\boldsymbol{\chi}_i$ ,  $\boldsymbol{\mu}^{p,i}$ , and  $\boldsymbol{\mu}^h$  are the weighting functions for the velocity  $\mathbf{u}$ , the pressure  $p$ , the translational velocity of a particle  $\mathbf{U}_i$ , the angular velocity of a particle  $\boldsymbol{\omega}_i$ , the Lagrange multiplier for the rigid-body constraint  $\boldsymbol{\lambda}^{p,i}$ , and the Lagrange multiplier for the periodic condition  $\boldsymbol{\lambda}^h$ , respectively.

In the combined weak form, the rigid-body motion of the particles is enforced by the constraint equation [Eq. (9)] using Lagrange multipliers  $\boldsymbol{\lambda}^{p,i}$  defined on both the particle boundary  $\partial P_i$  and the internal boundary  $\partial P'_i$  of the Janus particles [see Eqs. (15) and (17)]. We use biquadratic interpolation for the velocity, bilinear interpolation for the pressure, and linear interpolation for the Lagrange multipliers. The resulting matrix equation is solved by the same solver as used for the magnetic problem. The evolution equations for the position and the orientation of the particles, Eqs. (10) and (11), are solved by the same solution technique used in Ref. [37].

#### IV. VALIDATION OF THE NUMERICAL SCHEME

To validate the numerical scheme, a single-particle problem is used. The computational domain is a square chamber with the length of a side  $2h$ , filled with a circular Janus particle and a nonmagnetic fluid. The particle with the radius  $0.2h$  is located at the center of the domain with its orientation directed vertically, i.e.,  $\mathbf{q}_1 = \mathbf{j}$ , in the presence of an externally applied magnetic field,  $\bar{\mathbf{H}} = (\mathbf{i} + \mathbf{j})/\sqrt{2}$ . For validation, we use the following fixed material properties: The fluid viscosity is

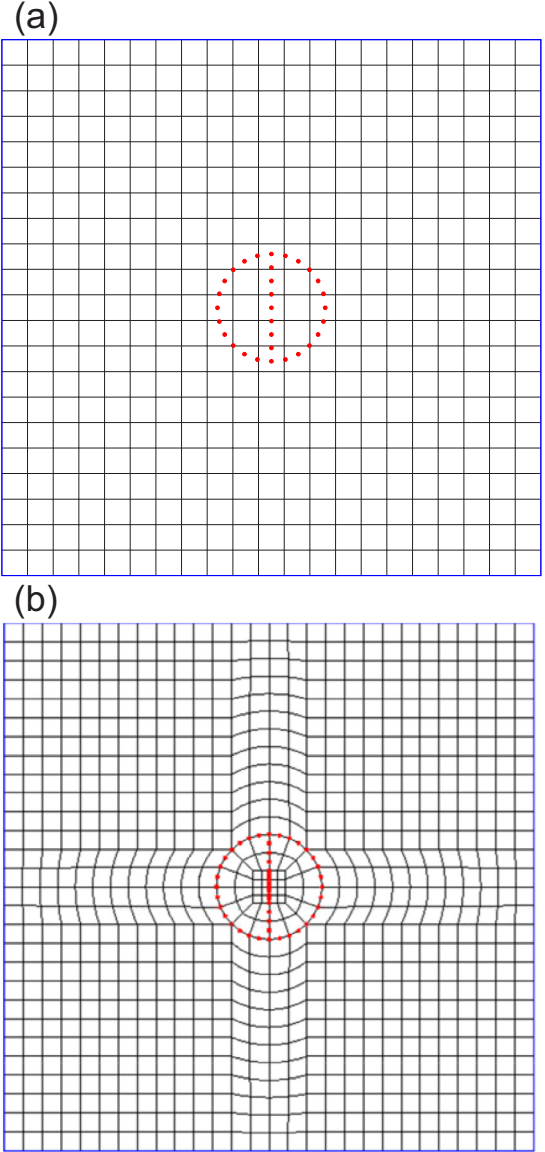


FIG. 2. Two meshes for a single particle problem for the validation of the numerical scheme. (a) Regular mesh and (b) boundary-fitted mesh.

$\eta = 0.01$ , the magnetic permeability of the magnetic material is  $\mu_p = 2\mu_0$ , i.e.,  $\chi_p = 1$ , and the magnetic permeability of nonmagnetic materials is set to  $\mu_0 = 1$ .

Since there is no analytic solution for the particulate flow with a circular Janus magnetic particle, we compare results obtained from a regular mesh [Fig. 2(a)] with those obtained from the corresponding boundary-fitted mesh [Fig. 2(b)]. The regular mesh is generated in such a way that both the outer boundary  $\partial P$  and the internal boundary  $\partial P'$  of the Janus particle do not coincide with element boundaries. In Fig. 2, dots are nodal points on the two boundaries ( $\partial P$  and  $\partial P'$ ) of the particle. In the boundary-fitted mesh problem, elements are generated such that the two boundaries of the particle coincide with the boundaries of the elements.

The convergence of the numerical solution is discussed using the rigid-body motion of the particle and the fluid velocity. We calculate the relative error in the angular velocity  $\omega$  of the particle  $\varepsilon_\omega$  and that of the velocity in the fluid domain  $\varepsilon_u$ , defined by

$$\varepsilon_\omega = \frac{|\omega - \omega_{ref}|}{|\omega_{ref}|}, \quad (19)$$

$$\varepsilon_u = \frac{|\mathbf{V} - \mathbf{V}_{ref}|}{|\mathbf{V}_{ref}|}. \quad (20)$$

In Eqs. (19) and (20), variables with the subscript “ref” are obtained from a boundary-fitted mesh problem and variables without the subscript from a problem for which the errors are calculated. Results obtained from the boundary-fitted mesh that is 32 times finer than the mesh shown in Fig. 2(b) are used as references for validation. The vector  $\mathbf{V}$  is a  $2n$ -dimensional vector, defined by  $\mathbf{V} = (\mathbf{u}_1, \mathbf{u}_2, \mathbf{u}_3, \dots, \mathbf{u}_n)$ , where  $\mathbf{u}_i$  denotes

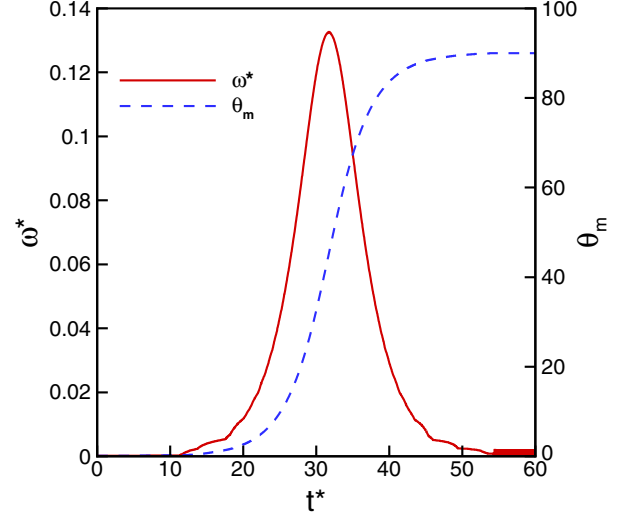


FIG. 4. Dimensionless angular velocity ( $\omega^* = \omega t_m$ ) and the orientation angle  $\theta_m$  with the nondimensional time ( $t^* = t/t_m$ ).

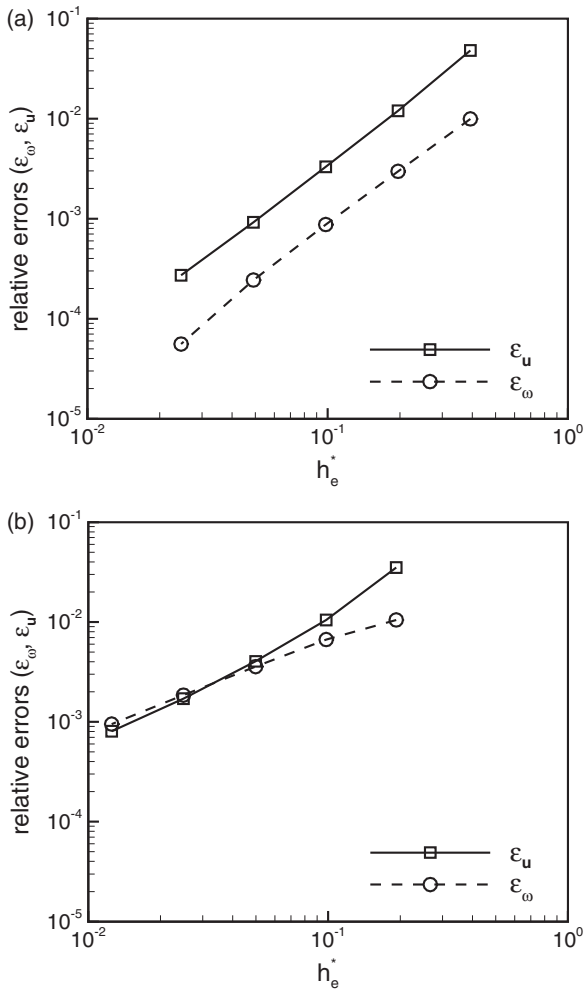


FIG. 3. Relative error of the angular velocity of the particle  $\varepsilon_\omega$  and that of the fluid velocity  $\varepsilon_u$  with mesh refinement. The abscissa is the element size scaled by the particle radius,  $h_e^* = h_e/a$ . (a) Errors in the boundary-fitted mesh problem; (b) errors in the regular mesh problem.

the velocity at the  $i^{\text{th}}$  node of the boundary-fitted mesh and  $n$  the number of the nodal points.

The two errors,  $\varepsilon_\omega$  and  $\varepsilon_u$ , as functions of the dimensionless mesh size ( $h_e^* = h_e/a$ ) are plotted in Fig. 3. The errors obtained from the boundary-fitted mesh problem show almost quadratic convergence with mesh refinement [see Fig. 3(a)]. As shown in Fig. 3(b), however, the convergence rates are almost linear in the case of the regular mesh problem, slower than those obtained from the boundary-fitted mesh problem. The slower convergence rate is thought to be caused by applying the magnetic forces, which are discontinuous at the interfaces between magnetic and nonmagnetic materials, to a regular mesh. Though one can obtain a more accurate solution by using the boundary-fitted mesh, continuous remeshing is required in that case, which is not an easy task for particles that form chains or clusters evolving continuously with time. All of the results that will be introduced in the following sections are computed using the regular mesh with the size  $h_e^* = 0.012$ , leading to an order of the errors less than  $10^{-3}$ . A more sophisticated numerical scheme based on the extended finite element method (XFEM) [41] is one of possible options to achieve higher accuracy and faster convergence rates in a magnetic particulate flow problem using a regular mesh.

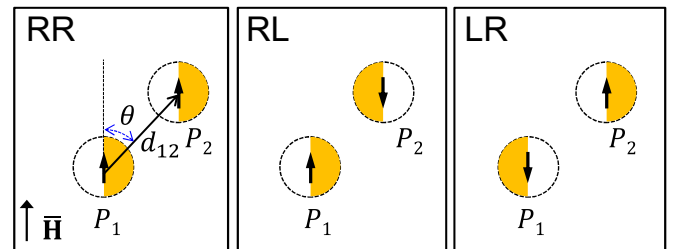


FIG. 5. Schematic illustration of two-particle problems with three initial configurations: RR, RL, and LR. The arrow in each particle indicates the orientation vector of the particle.

V. RESULTS

In this section, particle motions and the flow in single-, two-, and multiparticle problems will be investigated. Our main focus is on the effect of the particle orientation on particle motions and the fluid flow induced by the particle motions. Janus magnetic particles are suspended in a square periodic domain under the influence of a uniform magnetic field  $\vec{H}$  directed vertically, i.e.,  $\vec{H} = H_0 \mathbf{j}$ . The fluid flow is driven only by the particles actuated magnetically. The particle radius is fixed to  $a = 0.1h$  and the susceptibility of the magnetic material is  $\chi_p = 1$ , i.e.,  $\mu_p = 2\mu_0$ . All the results will be presented using dimensionless variables. The length has been made dimensionless with the particle radius  $a$  and the time with a magnetic time scale  $t_m = \eta/(\mu_0\beta^2 H_0^2)$ , where  $\beta$  is the effective polarization factor adopted from that of a spherical paramagnetic particle [37].

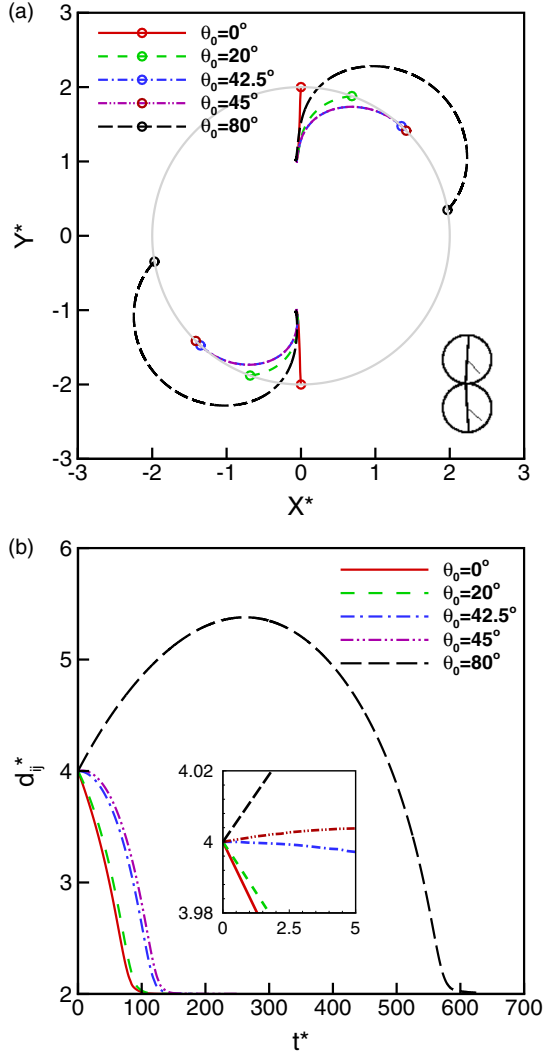


FIG. 6. Rigid-body motions of the two Janus particles with the RR configuration at the five initial angles  $\theta = 0^\circ, 20^\circ, 42.5^\circ, 45^\circ,$  and  $80^\circ$ . Initially, the centers of the particles are located on a circle of radius  $2a$  (gray circle). (a) Particle trajectories and (b) dimensionless distance between the two particles ( $d_{ij}^* = d_{ij}/a$ ) with time ( $t^* = t/t_m$ ).

A. The single-particle problem

We begin with a single-particle problem where the particle is initially located at the center of the domain. The initial particle orientation angle is set to  $\theta_m = 0.1^\circ$ . Figure 4 depicts the change of the orientation angle  $\theta_m$  and the dimensionless angular velocity of the particle,  $\omega^* = \omega t_m$ , with the dimensionless time  $t^* = t/t_m$ . Once the external field is applied, the particle begins to rotate counterclockwise due to the magnetic torque and is eventually aligned with the field direction. The driving force is generated by the magnetic anisotropy of the particle, creating a nonuniform field around the particle. Note that, in the case of a single circular (or spherical in 3D) paramagnetic particle with uniform magnetic property, no magnetic torque acts on the particle. The angular velocity varies with the particle orientation and its maximum value occurs at  $\theta_m = 45^\circ$ , where the magnetic torque acting on the particle is also maximum. When the particle orientation is either vertical or parallel to the external field, the particle cannot rotate.

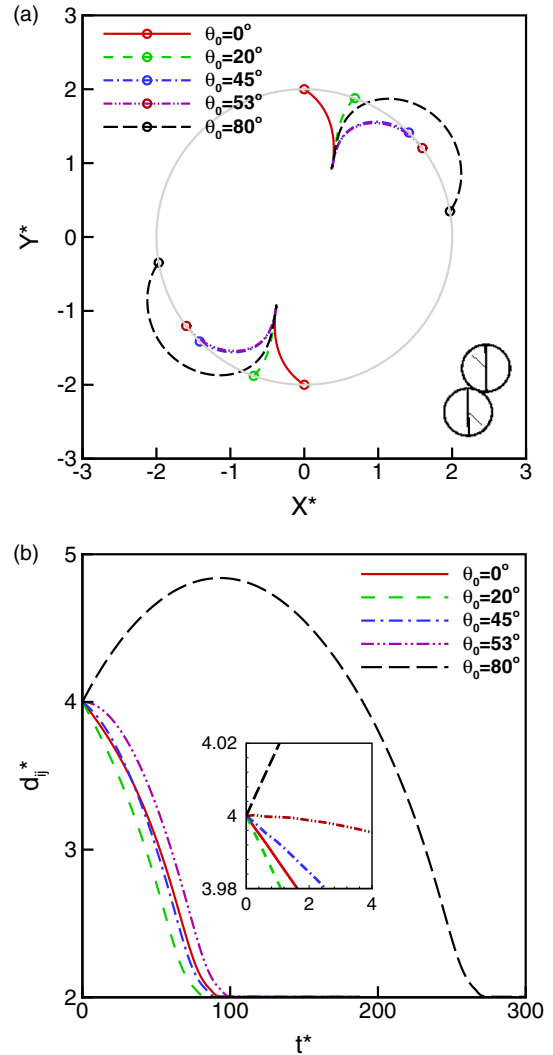


FIG. 7. Rigid-body motions of the two Janus particles with the RL configuration at the five initial angles  $\theta = 0^\circ, 20^\circ, 45^\circ, 53^\circ,$  and  $80^\circ$ . (a) Particle trajectories and (b) dimensionless distance between the two particles  $d_{ij}^*$  with time  $t^*$ .

### B. Interaction between two Janus magnetic particles

It is well known that the interaction forces between two magnetic particles in a uniform magnetic field are dependent on the angle  $\theta$  between the field direction and the line connecting the centers of the two particles [42]. Based on the point-dipole approximation, the critical angle  $\theta_c$  separating the nature of the magnetic interaction (either attractive or repulsive) is  $\cos^{-1}(1/\sqrt{3}) \approx 54.7^\circ$  for two spherical paramagnetic particles [42], while for two circular paramagnetic particles, it is numerically found to be  $45^\circ$  [33,43]. The force is attractive at an angle less than  $\theta_c$ , but repulsive at an angle larger than  $\theta_c$ . The critical angle can also be affected by the interparticle distance  $d_{12}$  due to the variation of the magnetic field around the particles, as the distance changes [37].

To examine the magnetic interaction between two Janus particles affected by the initial configuration, we choose two-particle problems with three initial configurations, RR, RL, and LR (see Fig. 5). Here it is assumed that each particle is initially aligned with the field direction, i.e.,  $\mathbf{q}_i = \mathbf{j}$  or

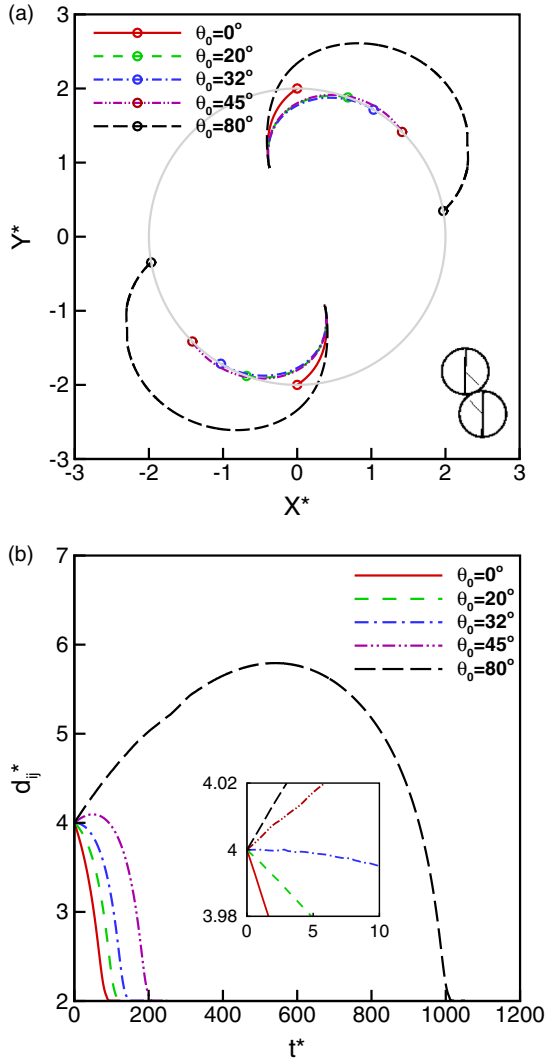


FIG. 8. Rigid-body motions of the two Janus particles with the LR configuration at the five initial angles  $\theta = 0^\circ, 20^\circ, 32^\circ, 45^\circ,$  and  $80^\circ$ . (a) Particle trajectories and (b) dimensionless distance between the two particles  $d_{ij}^*$  with time  $t^*$ .

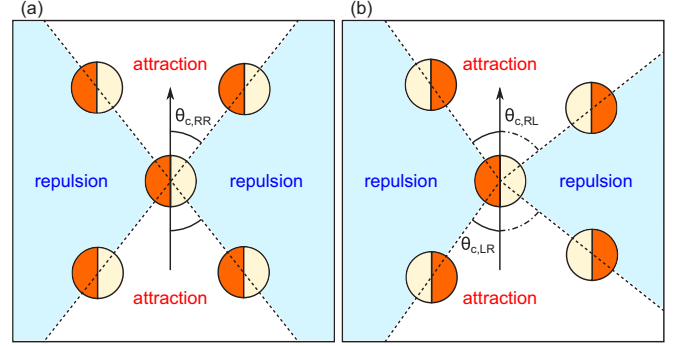


FIG. 9. Magnetic interaction between two particles in a uniform magnetic field directed vertically. For the three configurations, the critical angles separating the nature of magnetic interaction are  $\theta_{c,RR} \approx 42.5^\circ$ ,  $\theta_{c,RL} \approx 53.5^\circ$ , and  $\theta_{c,LR} \approx 32^\circ$ . (a) RR configuration and (b) RL and LR configurations.

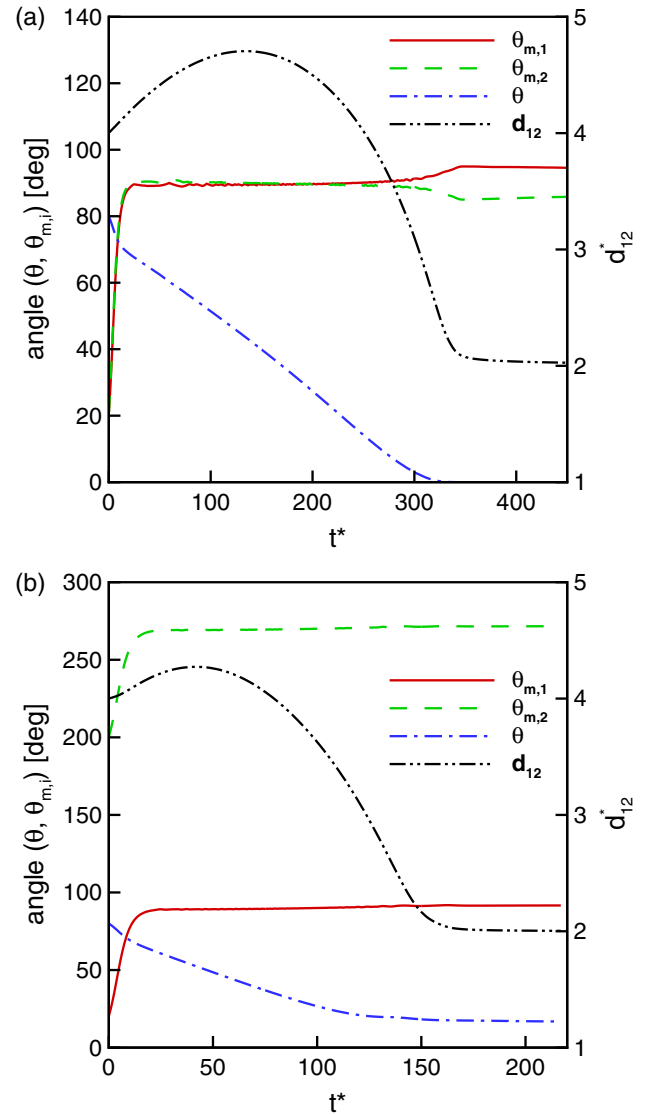


FIG. 10. Change of the angles ( $\theta, \theta_{m,1}$ , and  $\theta_{m,2}$ ) and the dimensionless interparticle distance  $d_{ij}^*$  with time  $t^*$  for two configurations; (a) RR configuration with  $\theta_{m,1} = \theta_{m,2} = 20^\circ$  and (b) RL configuration with  $\theta_{m,1} = 20^\circ$  and  $\theta_{m,2} = 200^\circ$ . Initially, the distance  $d_{ij}^* = 4$  and the angle  $\theta$  is  $80^\circ$ .

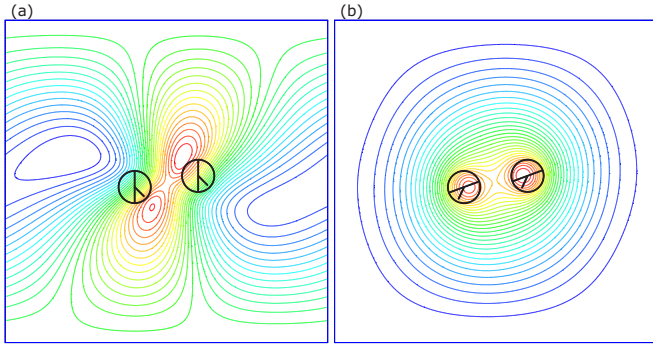


FIG. 11. Instantaneous streamlines in RR configurations at (a)  $\theta_m = 90^\circ$  and (b)  $\theta_m = 20^\circ$ . The angle  $\theta$  between two vectors,  $\vec{H}$  and  $X_2 - X_1$ , is  $80^\circ$  in the two figures.

$q_i = -j$ . The initial configuration of a particle  $P_i$  is determined by its orientation vector. If the vector is directed upward, i.e.,  $q_i = j$ , and the magnetic area is on the right side of the particle, then this configuration is assigned the letter “R,” but if directed downward, i.e.,  $q_i = -j$ , and the magnetic area is on the left side of the particle, it is assigned the letter “L.” In the RL configuration, for example, the two orientation vectors are defined by  $q_1 = j$  and  $q_2 = -j$ . Initially, the distance ( $d_{12}$ ) between the particles is fixed to be  $4a$ . In the following, the magnetic interaction between the two particles is characterized in terms of the angle  $\theta$  initially in the range  $0^\circ \leq \theta < 90^\circ$  and the initial orientation of the particles.

The trajectory of the particles and the interparticle distance with time at several initial angles are plotted in Figs. 6–8. In RR configurations, the particles are finally assembled into a straight configuration depicted in the lower right of Fig. 6(a). The rigid-body motions of the Janus particles with the RR configuration are similar to those of isotropic magnetic particles reported in a previous study [33]. However, the critical angle  $\theta_c$  differs from that found in the isotropic magnetic particles. The

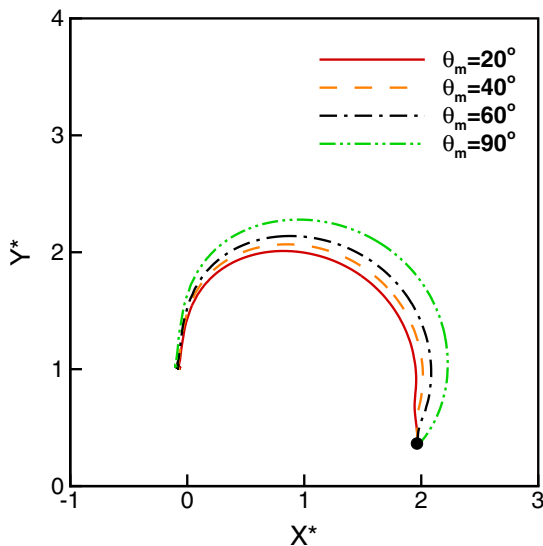


FIG. 12. Trajectories of the particle  $P_2$  in the RR configuration with  $\theta_m = 20^\circ, 40^\circ, 60^\circ$ , and  $90^\circ$ . The initial angle between the field and the line connecting the center of the particles is  $\theta_0 = 80^\circ$ .

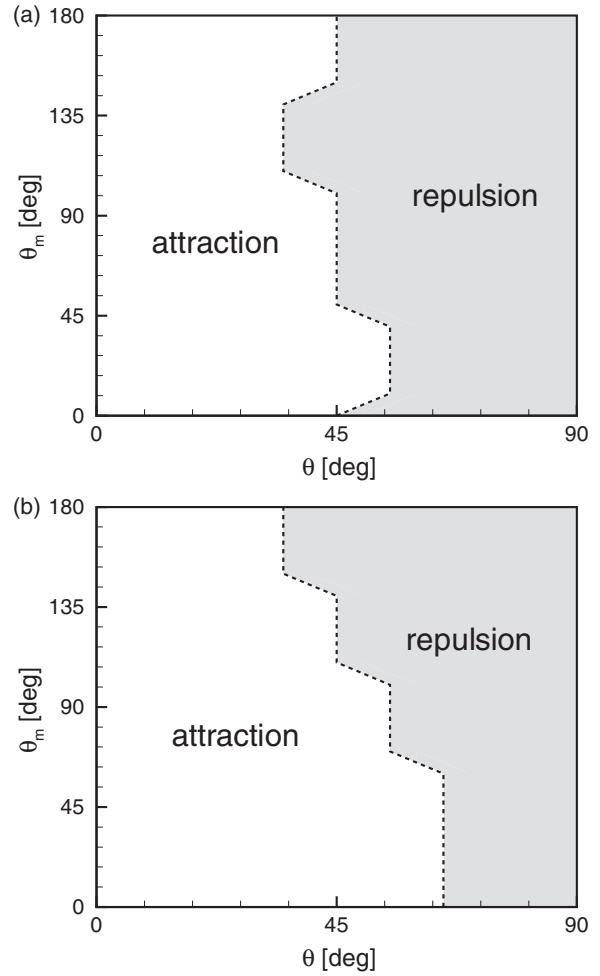


FIG. 13. Maps showing the magnetic interaction between two Janus particles characterized in terms of  $\theta$  and  $\theta_m$  at the two configurations. (a) RR and (b) RL.

critical angle in this configuration is found to be approximately  $\theta_{c,RR} \approx 42.5^\circ$ . Though the two-particle chain is aligned with the field direction, interestingly, the two orientation vectors,  $q_1$  and  $q_2$ , are neither parallel to each other nor aligned with the field direction but tilted slightly after joining together, which is similar to that observed experimentally [9]. At

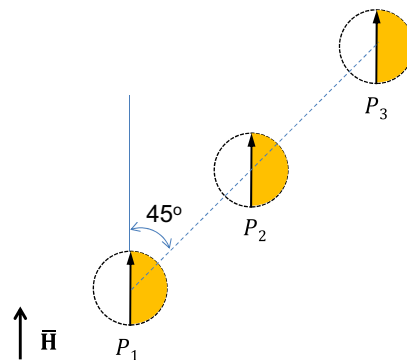


FIG. 14. A three-particle problem with a linear RRR configuration. The angle between the externally applied field  $\vec{H}$  and the line connecting the centers of the particles is  $45^\circ$ .

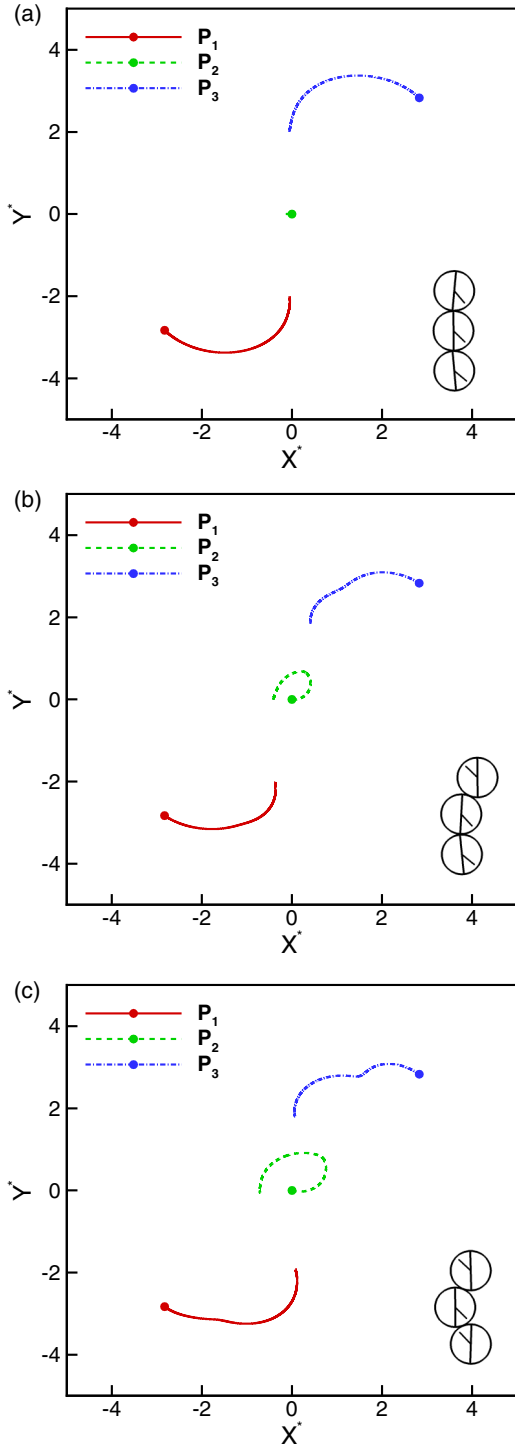


FIG. 15. Trajectories of the three particles for three initial configurations, (a) RRR, (b) RRL, and (c) LRL. Solid circles in the plots denote the initial locations of the particles. The final conformation of the three-particle chain is shown in the lower right part of each plot.

this final conformation, the magnetic energy  $W_m$ , defined by  $W_m = \int (\mathbf{B} \cdot \mathbf{H})/2d\Omega$ , is found to be at a minimum.

Figures 7 and 8 depict the trajectories of the particles and the time history of the inter-particle distance in the RL and LR configurations, respectively. As shown in the lower

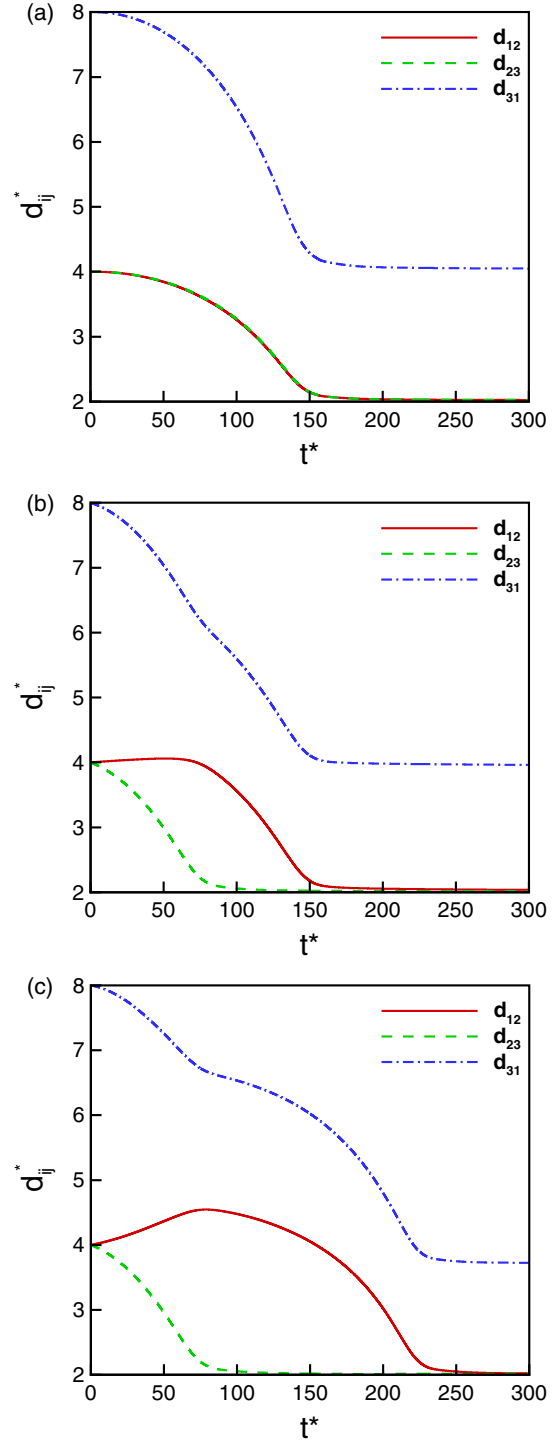


FIG. 16. Dimensionless interparticle distance  $d_{ij}^*$  with time  $t^*$  for the three initial configurations, (a) RRR, (b) RRL, and (c) LRL. Here  $d_{ij}^* = d_{ij}/a$  and  $t^* = t/t_m$ .

right corner of Fig. 7(a) and Fig. 8(a), inclined two-particle chains are formed in both cases. The critical angle in the RL configuration is  $\theta_{c,RL} \approx 53^\circ$ , while that in the LR configuration is found to be  $\theta_{c,LR} \approx 32^\circ$ . The two critical angles ( $\theta_{c,RL}$  and  $\theta_{c,LR}$ ) show notable deviations compared with that of two isotropic paramagnetic particles. Since, at a given value of  $\theta$ , the distance between two magnetic areas is the shortest in

the RL configuration, the interaction force is higher than that in the other two cases, leading to a faster assembly of the particles. Note that, in the RL configuration, the time required to form a chain at  $\theta_0 = 20^\circ$  and  $45^\circ$  is shorter than that at  $\theta_0 = 0^\circ$  [see Fig. 7(b)], which is not the case in the RR and LR configurations.

Due to the magnetic anisotropy of the particles, each configuration has a unique critical angle and a unique final conformation, which completely differ from those obtained from a corresponding counterpart with isotropic magnetic particles. Magnetic interactions between two circular Janus magnetic particles in the three initial configurations are graphically summarized in Fig. 9. The maps describe the magnetic interaction between one particle ( $P_1$ ) (fixed at the center) and the other particle ( $P_2$ ) around the fixed one. If the second particle  $P_2$  is positioned in the shaded region in the maps, then the interaction is repulsive, otherwise the interaction is attractive. From the simulations introduced, we show that, in addition to the angle  $\theta$  and the interparticle distance  $d_{12}$ , the orientation of the Janus particles is also a factor with an influence on the two-particle interaction and resulting particle motions.

### C. Effect of the initial orientation on two-particle interaction

In this section, the effect of the orientation of each particle on the two-particle interaction and the fluid flow are investigated in more detail by extending the definition of the “R” and “L” configurations. Two-particle problems for RR and RL configurations are chosen as representative examples. The problems are the same as those introduced in Sec VB except that the particles are initially not aligned with the externally applied magnetic field directed vertically. The configuration of a particle  $P_i$  with the orientation angle in  $0^\circ < \theta_{m,i} < 180^\circ$  is assigned “R,” while it is assigned “L” if  $180^\circ < \theta_{m,i} < 360^\circ$ . For a specific orientation angle  $\bar{\theta}_m$ , the particle orientation angles are set to  $\theta_{m,1} = \theta_{m,2} = \bar{\theta}_m$  for the RR configuration, and  $\theta_{m,1} = \bar{\theta}_m$  and  $\theta_{m,2} = \bar{\theta}_m + 180^\circ$  for the RL configuration. To see the influence of the initial orientation on particle motions, we solve the two-particle problem by changing the two angles,  $\bar{\theta}_m$  and  $\theta_0$ .

As an example, we introduce rigid-body motions of the particles for the two configurations with the initial angle  $\theta_0 = 80^\circ$ . Figure 10 shows the evolution of the orientation angles ( $\theta_{m,1}$  and  $\theta_{m,2}$ ), the interparticle distance  $d_{12}$ , and the angle  $\theta$  between the field and the line-of-centers of the particles with  $\bar{\theta}_m = 20^\circ$ . Upon applying the field, each particle

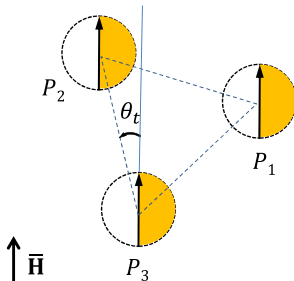


FIG. 17. A three-particle problem with a triangular RRR configuration.

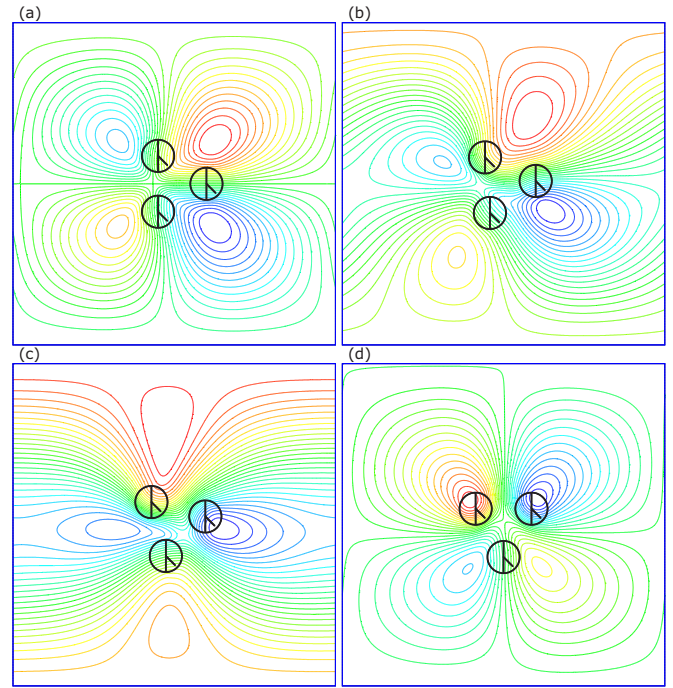


FIG. 18. Snapshots of the streamlines obtained from a three-particle problem with triangular RRR configurations: (a)  $\theta_t = 0^\circ$ , (b)  $\theta_t = 5^\circ$ , (c)  $\theta_t = 15^\circ$ , and (d)  $\theta_t = 30^\circ$ .

rotates and is aligned with the field direction in the early stage of the rigid-body motion, due to the magnetic torque induced by magnetic anisotropy of the particle. Then the two particles show similar rigid-body motions to those observed in Sec. VB, eventually forming a two-particle chain. In both

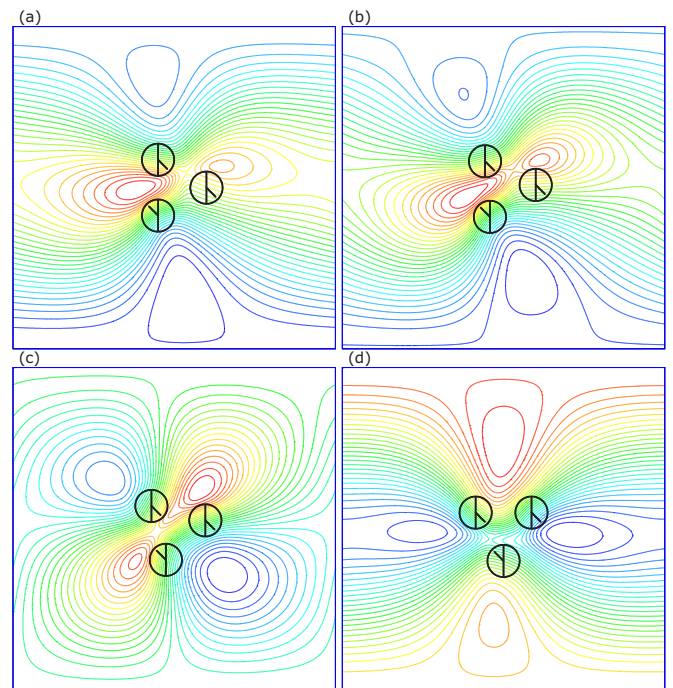


FIG. 19. Snapshots of the streamlines obtained from a three-particle problem with triangular RRL configurations: (a)  $\theta_t = 0^\circ$ , (b)  $\theta_t = 5^\circ$ , (c)  $\theta_t = 15^\circ$ , and (d)  $\theta_t = 30^\circ$ .

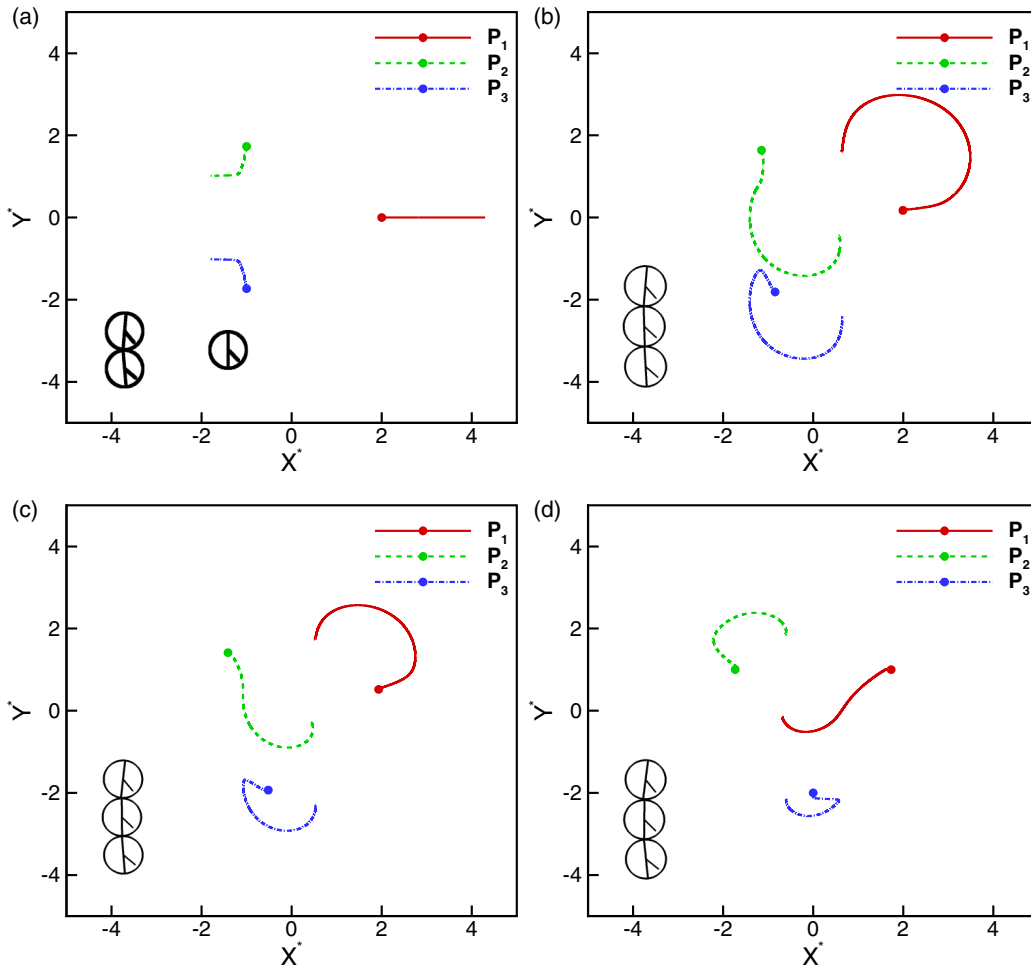


FIG. 20. Trajectories of the particles obtained from a three-particle problem with triangular RRR configurations: (a)  $\theta_t = 0^\circ$ , (b)  $\theta_t = 5^\circ$ , (c)  $\theta_t = 15^\circ$ , and (d)  $\theta_t = 30^\circ$ . Solid circles indicate initial positions of the particles. The final conformation of the three-particle chain is shown in the lower-left part of each plot.

configurations, the time scale of the rotational motion of the particles is much shorter than that of the translational motion. Once the particle orientations become parallel to the field direction, the particles are irrotational in the RL configuration. In the RR configuration, however, the particles show rotational motions just before joining together to form a two-particle chain depicted in Fig. 6(a).

To demonstrate the change in hydrodynamics affected by particle orientation, we plot instantaneous streamlines at  $\theta = 80^\circ$  for two RR configurations with  $\bar{\theta}_m = 20^\circ$  and  $90^\circ$  (see Fig. 11). When the particles are aligned with the field direction (i.e.,  $\bar{\theta}_m = 90^\circ$ ), vortical flows around the particles are induced purely by the repulsive translational motion of the particles [see Fig. 11(a)], which is similar to those obtained with isotropic magnetic particles [43]. In the other case with  $\bar{\theta}_m = 20^\circ$ , however, a completely different flow pattern is obtained, as shown in Fig. 11(b). Inside a globally rotating flow, two small corotating flows exist due to spinning of the particles. In this case, the flow is mostly induced by the spinning motion of the particles rather than translational motions of the particles. The rotating flows at  $\bar{\theta}_m = 20^\circ$  lead to a faster decrease in the angle  $\theta$  compared to the case with  $\bar{\theta}_m = 90^\circ$ , subsequently resulting in

a faster transition from the repulsive interaction to the attractive interaction in the two-particle interaction problem. Figure 12 depicts changes in the trajectory of the particle  $P_2$  at the four orientation angles,  $\bar{\theta}_m = 20, 45, 80,$  and  $90^\circ$ . The smaller  $\bar{\theta}_m$  the shorter the path of the particles, which is due to the combined effect of the hydrodynamic interaction and the magnetic interaction dependent on the orientation of the particles.

Given the externally applied magnetic field, the angle  $\theta$  and the orientation angle  $\bar{\theta}_m$  are key factors that determine the magnetic interaction between two Janus particles. To characterize the magnetic interaction governed by such factors, simulations are conducted in a wide range of  $\theta$  and  $\bar{\theta}_m$ . The angle  $\theta$  is varied from  $0^\circ$  to  $90^\circ$  and the orientation angle  $\bar{\theta}_m$  from  $0^\circ$  to  $180^\circ$  with an increment of  $10^\circ$ . Depicted in Fig. 13 are maps showing the nature of the magnetic interaction affected by  $\theta$  and  $\bar{\theta}_m$  for the RR and RL configurations. In each plot, the forces working on the particles are attractive in the region left to the dashed line, but repulsive in the region right to the dashed line. The critical angle, separating the nature of the magnetic interaction, is found to lie between  $35^\circ$  and  $55^\circ$  for the RR configuration. In the RL configuration, the critical angle is in between  $35^\circ$  and  $65^\circ$ .

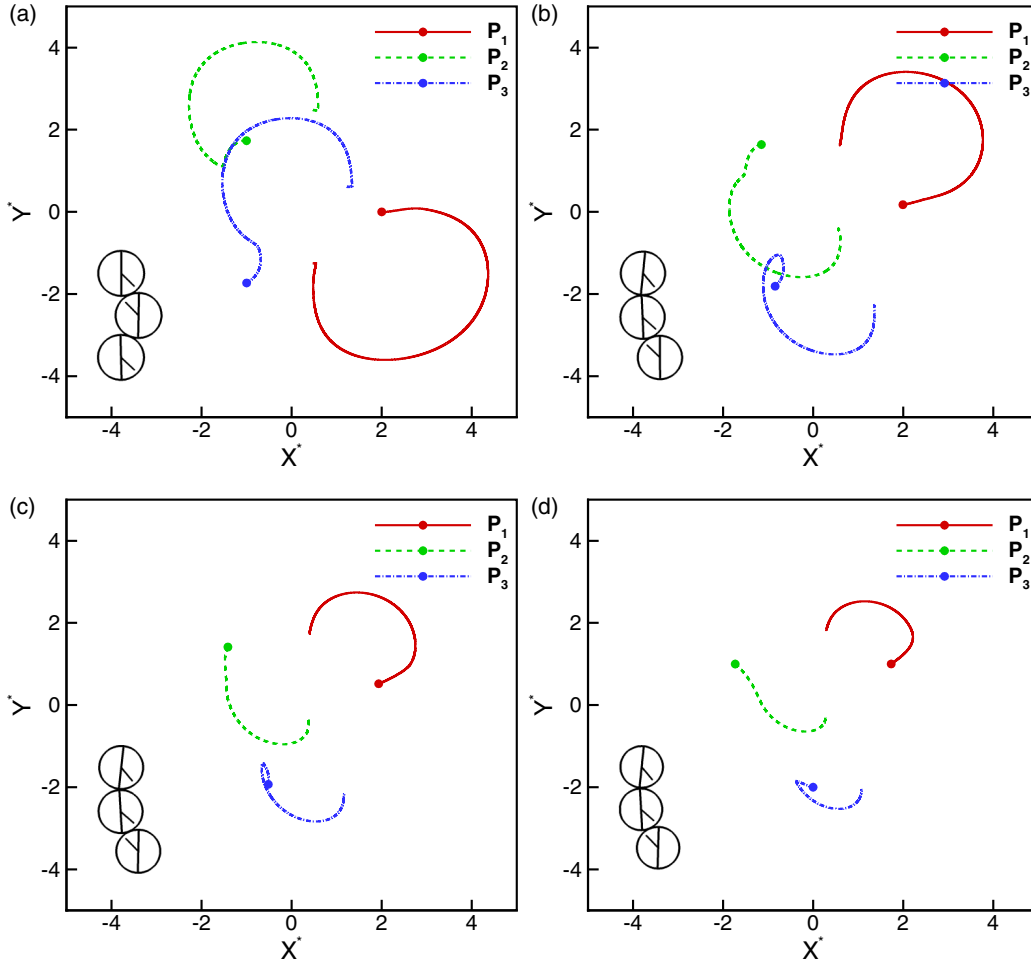


FIG. 21. Trajectories of the particles obtained from a three-particle problem with triangular RRL configurations: (a)  $\theta_t = 0^\circ$ , (b)  $\theta_t = 5^\circ$ , (c)  $\theta_t = 15^\circ$ , and (d)  $\theta_t = 30^\circ$ .

#### D. Three-particle interactions

Now we extend our interest to multiparticle problems. First, a three-particle problem is solved for RRR, LRL, and RRL configurations. Figure 14 shows an RRR configuration as an example. Each particle is initially equidistant from its neighboring particle(s) with its orientation vector parallel to the magnetic field directed vertically. In the beginning, the distance  $d_{ij}$  between two adjacent particles,  $P_i$  and  $P_j$ , is set to  $4a$  and the angle  $\theta_{ij}$  between the line-of-centers of the two particles and the magnetic field is  $45^\circ$  for all the cases. The susceptibility of the magnetic material is fixed to  $\chi_p = 1$ .

Figure 15 depicts the trajectories of the particles and the final three-particle chain (shown in the lower-right part of each plot) for the three configurations. We also plot the dimensionless distance  $d_{ij}^*$  between two particles ( $P_i$  and  $P_j$ ) with the dimensionless time  $t^*$  (see Fig. 16). In the RRR configuration, the second particle ( $P_2$ ) remains stationary and the other two particles move towards  $P_2$ , eventually forming a linear chain. While, in the other two configurations (RRL and LRL), staggered chains are formed, implying that the final chain structure is affected by the initial orientation of the particles. A pair of particles ( $P_2$  and  $P_3$ ) for which the distance between

two magnetic domains is the shortest join together to form a two-particle chain. This is due to a stronger magnetic attraction than that of the other pairs. Then the third one is joined to the two-particle chain and a three-particle chain is formed. In the LRL configuration, the repulsive motion between  $P_1$  and  $P_2$  in the early stage of particle motion is stronger than that of the RRL configuration. Accordingly, it takes longer to form a three-particle chain, compared with the case in the RRL configuration.

Next introduced is another three-particle problem, where the three particles are initially in an equilateral triangular configuration with the centers of the particles located at the vertices of the triangle. Kang and Suh [43] studied three-particle interactions among circular paramagnetic particles for the same triangular configurations as used in this study. Figure 17 shows a three-particle problem with a triangular RRR configuration. The origin of the coordinate system is at the center of a circumcircle passing through the three vertices of the triangle. The circumdiameter is  $4a$ , thus  $d_{ij} = 2\sqrt{3}a$ . As for the initial orientations of the particles, we choose two configurations, RRR and RRL. To investigate the effect of the initial positions of the particles on particle motions, four cases classified by the angle  $\theta_t$  are selected. Here  $\theta_t$  is the angle

between two vectors,  $\vec{H}$  and  $X_2 - X_3$ , in this study ranging from  $0^\circ$  to  $30^\circ$ .

Figures 18 and 19 depict the snapshots of streamlines in the beginning for the flows induced by actuated particles in the RRR and RRL configurations, respectively. In the RRR configuration with  $\theta_t = 0^\circ$ , four vortical flows that are symmetric with respect to the  $x$  axis are observed [see Fig. 18(a)]. As the angle  $\theta_t$  increases, the symmetry in the particle configuration is broken and the flow field gets distorted due to the magnetic interactions dependent on the particle orientations. At  $\theta_t = 30^\circ$ , the triangle formed by the centers of the particles is symmetric with respect to the  $y$  axis [Fig. 18(d)]. If the orientation of each particle is considered, however, the configuration itself is not symmetric, leading to a flow field with broken symmetry, which differs from the case with uniform magnetic particles. Comparing a flow field obtained from the RRL configuration with that from the corresponding RRR configuration, one can find that the two flow fields completely differ from each other. The reversed orientation of the third particle  $P_3$  leads to changes in the magnetic interactions among the particles and subsequently changes in the fluid flow driven by the actuated particles.

Depicted in Figs. 20 and 21 are the trajectories and final conformations of the particles for the two triangular configurations. In the RRR configuration, the particles form a linear three-particle chain, except for the case with  $\theta_t = 0^\circ$  where a two-particle chain and a separate particle keep moving away [see Fig. 20(a)]. It should be noted that, at  $\theta_t = 5^\circ$  and  $15^\circ$ , the sequence of particles constituting a chain is the same. However, the sequence of particles at  $\theta_t = 30^\circ$  is in a different order, compared with the other two cases. While, in the RRL configuration, the particles form three-particle chains in all the cases, the final chain conformation and the sequence of the particles at  $\theta_t = 0^\circ$  differs from the other three cases.

The results obtained from the three-particle problems clearly manifest the influence of the orientations and the relative positions of the Janus particles on the magnetic interactions, the chain conformation, and the flow field induced by the particle motions.

### E. Chain formation

Motivated by the experimental study conducted by Yuet *et al.* [9], we finally solve a multiparticle problem that is related to one of their experimental results depicted in Fig. 22(a). In this problem, particles are randomly distributed in the chamber under the influence of the uniform magnetic field directed vertically. Figure 22(b) shows the final conformation of the particles with  $N = 30$ , resulting in straight and staggered chains. At a higher particle concentration with  $N = 50$ , complex chains with branches are also formed [see Fig. 22(c)]. The detailed structure of each chain is highly dependent on the initial configuration of the particles. The two-particle chain in the upper-left corner of Fig. 22(a) is similar to the numerically predicted one [shown in Fig. 6(a)] in the way that the internal interfaces of the particles are not aligned with the field direction. Even though our numerical scheme is two dimensional, we are able to reproduce similar

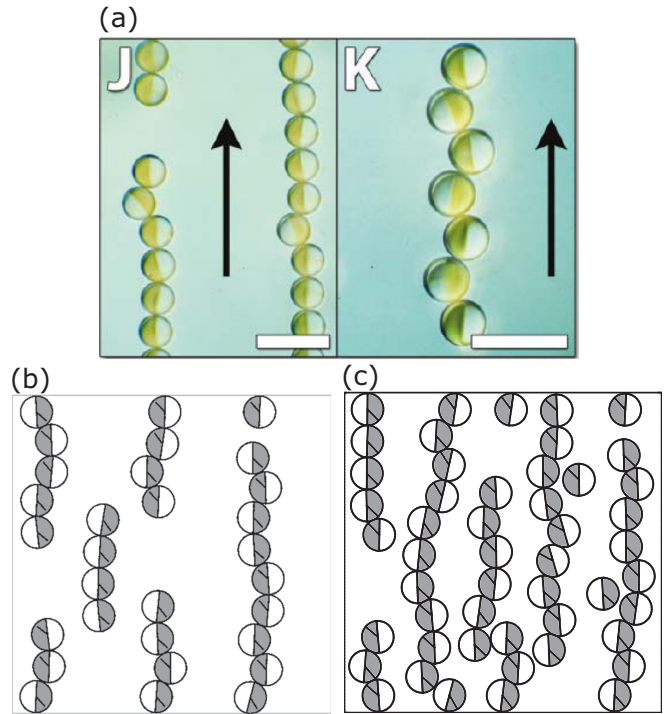


FIG. 22. Chain formation in a multiparticle problem with the externally applied magnetic field directed vertically. (a) Chain structures observed experimentally by Yuet *et al.* [9] (Reprinted with permission from Ref. [9]. Copyright 2010 American Chemical Society.) and chain structures obtained from a numerical simulation with (b)  $N = 30$  and (c)  $N = 50$ .

chain structures to those observed experimentally by Yuet *et al.* [9].

## VI. CONCLUSION

We numerically investigated the magnetic interaction of circular Janus magnetic particles suspended in a viscous liquid in the presence of an externally applied uniform magnetic field. To solve particulate flows with Janus particles, a previously developed direct simulation scheme was enhanced to be able to treat the magnetic anisotropy of the particles. In validation of the numerical scheme, it was shown that the solution converged with mesh refinement. Though the developed numerical scheme has been applied to flows with circular Janus magnetic particles, it can be extended to problems with noncircular magnetic particles, computationally intensive three-dimensional problems, and viscoelastic flows with suspended Janus particles.

If the orientation of a Janus particle is neither parallel nor vertical to the field direction, contrary to a single circular isotropic paramagnetic particle, then the magnetic torque caused by magnetic anisotropy acts on the Janus particle and induces the rotational motion of the particle. As for two-particle interaction, the critical angle separating the nature of magnetic interaction (i.e., attractive or repulsive) and the trajectories of the particles are significantly affected by the configuration of the particles. A specific configuration results in a unique final chain conformation that is not

observed in case of isotropic particles. When the initial orientations of the particles are not aligned with the field, the time scale of the rotational motion of the particles is found to be much shorter than that of the translation motion caused by the magnetic interaction. Given spatial positions of the particles, the differences in the orientation of each particle lead to notable changes in the nature of magnetic interaction, the particle trajectories, the fluid flow induced by particle motions, and the final conformation of the chain

structures. Using a multiparticle problem, we were able to reproduce similar Janus particle chains to those observed experimentally.

#### ACKNOWLEDGMENTS

This research was supported by the National Research Foundation of Korea (NRF), funded by the Korean Government (Grant No. 2010-0004802, 2015R1D1A1A01057691).

- 
- [1] M. A. Gijs, *Microfluid. Nanofluid.* **1**, 22 (2004).  
 [2] N. Pamme, *Lab. Chip.* **6**, 24 (2006).  
 [3] R. Ganguly and I. K. Puri, *Wiley Interdiscip. Rev.-Nanomed. Nanobiotechnol.* **2**, 382 (2010).  
 [4] A. van Reenen, A. M. de Jong, J. M. J. den Toonder, and M. W. J. Prins, *Lab Chip* **14**, 1966 (2014).  
 [5] S.-M. Yang, S.-H. Kim, J.-M. Lim, and G.-R. Yi, *J. Mater. Chem.* **18**, 2177 (2008).  
 [6] K. J. Lee, J. Yoon, and J. Lahann, *Curr. Opin. Colloid Interface Sci.* **16**, 195 (2011).  
 [7] A. Walther and A. H. E. Müller, *Soft Matter* **4**, 663 (2008).  
 [8] C. J. Behrend, J. N. Anker, B. H. McNaughton, and R. Kopelman, *J. Magn. Magn. Mater.* **293**, 663 (2005).  
 [9] K. P. Yuet, D. K. Hwang, R. Haghgooie, and P. S. Doyle, *Langmuir* **26**, 4281 (2010).  
 [10] H. Xie, Z.-G. She, S. Wang, G. Sharma, and J. W. Smith, *Langmuir* **28**, 4459 (2012).  
 [11] B. J. Park and D. Lee, *Acs Nano* **6**, 782 (2011).  
 [12] A. Wolf, A. Walther, and A. H. Müller, *Macromolecules* **44**, 9221 (2011).  
 [13] A. Boymelgreen, G. Yossifon, S. Park, and T. Miloh, *Phys. Rev. E* **89**, 011003 (2014).  
 [14] I. Kretzschmar and J. H. K. Song, *Curr. Opin. Colloid Interface Sci.* **16**, 84 (2011).  
 [15] A. Walther and A. H. E. Müller, *Chem. Rev.* **113**, 5194 (2013).  
 [16] D. J. Klingenberg, *AIChE J.* **47**, 246 (2001).  
 [17] F. D. Goncalves, J.-H. Koo, and M. Ahmadi, *Shock Vibration Digest* **38**, 203 (2006).  
 [18] D. Zerrouki, J. Baudry, D. Pine, P. Chaikin, and J. Bibette, *Nature* **455**, 380 (2008).  
 [19] S. K. Smoukov, S. Gangwal, M. Marquez, and O. D. Velev, *Soft Matter* **5**, 1285 (2009).  
 [20] L. Zhang, F. Zhang, W.-F. Dong, J.-F. Song, Q.-S. Huo, and H.-B. Sun, *Chem. Commun.* **47**, 1225 (2011).  
 [21] Y. Liu, W. Li, T. Perez, J. D. Gunton, and G. Brett, *Langmuir* **28**, 3 (2011).  
 [22] S. Sacanna, L. Rossi, and D. J. Pine, *J. Am. Chem. Soc.* **134**, 6112 (2012).  
 [23] B. Ren, A. Ruditskiy, J. H. K. Song, and I. Kretzschmar, *Langmuir* **28**, 1149 (2012).  
 [24] J. Yan, S. C. Bae, and S. Granick, *Soft Matter* **11**, 147 (2015).  
 [25] Y. Gao, M. A. Hulslen, T. G. Kang, and J. M. J. den Toonder, *Phys. Rev. E* **86**, 041503 (2012).  
 [26] R. Fantoni, A. Giacometti, F. Sciortino, and G. Pastore, *Soft Matter* **7**, 2419 (2011).  
 [27] B. Li, Y.-L. Zhu, H. Liu, and Z.-Y. Lu, *Phys. Chem. Chem. Phys.* **14**, 4964 (2012).  
 [28] Y. Iwashita and Y. Kimura, *Soft Matter* **9**, 10694 (2013).  
 [29] T. Vissers, Z. Preisler, F. Smallenburg, M. Dijkstra, and F. Sciortino, *J. Chem. Phys.* **138**, 164505 (2013).  
 [30] M. Sobrino Fernández, V. R. Misko, and F. M. Peeters, *Phys. Rev. E* **89**, 022306 (2014).  
 [31] M. Mohammadi, E. D. Larson, J. Liu, and R. G. Larson, *J. Chem. Phys.* **142**, 024108 (2015).  
 [32] T. G. Kang, M. A. Hulslen, P. D. Anderson, J. M. J. den Toonder, and H. E. H. Meijer, *Phys. Rev. E* **76**, 066303 (2007).  
 [33] T. G. Kang, M. A. Hulslen, J. M. den Toonder, P. D. Anderson, and H. E. Meijer, *J. Comput. Phys.* **227**, 4441 (2008).  
 [34] Y. Suh and S. Kang, *J. Eng. Math.* **69**, 25 (2011).  
 [35] S. Kang and Y. K. Suh, *Int. J. Numer. Meth. Fluids* **67**, 58 (2011).  
 [36] T. G. Kang, M. A. Hulslen, and J. M. J. den Toonder, *Phys. Fluids* **24**, 042001 (2012).  
 [37] T. G. Kang, Y. Gao, M. A. Hulslen, J. M. den Toonder, and P. D. Anderson, *Comput. Fluids* **86**, 569 (2013).  
 [38] J. Jin, *The Finite Element Method in Electromagnetics* (John Wiley & Sons Inc, New York, 2002).  
 [39] W. R. Hwang, M. A. Hulslen, and H. E. H. Meijer, *J. Comput. Phys.* **194**, 742 (2004).  
 [40] I. S. Duff, *ACM Trans. Math. Softw.* **30**, 118 (2004).  
 [41] Y. Choi, M. Hulslen, and H. Meijer, *J. Non-Newtonian Fluid Mech.* **165**, 607 (2010).  
 [42] R. G. Larson, *The Structure and Rheology of Complex Fluids* (Oxford University Press, New York, 1999).  
 [43] S. Kang and Y. Suh, *J. Fluids Struct.* **27**, 266 (2011).